A Dynamic Energy-Based Hysteresis Model for Pulsed-Operated Fast-Ramping Magnets

Dominik Moll[1], Laura A. M. D'Angelo[1], Herbert De Gersem[1], Fulvio Boattini[2], Luca Bottura[2], Marco Gast[3]
[1]Institute for Accelerator Science and Electromagnetic Fields, TU Darmstadt, Germany
[2]CERN, Geneva, Switzerland
[3]Karlsruhe Institute for Technology, Germany

Due to the strongly nonlinear behavior of ferromagnetic yokes, the numerical analysis of fast-ramping magnets is highly cumbersome and, therefore, in practice overly simplified by means of anhysteretic material descriptions and a posteriori loss formulae. This paper establishes the use of a dynamic ferromagnetic model combining a preconditioned energy-based hysteresis description and a thin-sheet eddy-current model in time-domain. The model was successfully employed in the analysis of a normal-conducting bending magnet in order to precisely calculate losses and fields.

***Index Terms*—accelerator magnets, eddy currents, finite element simulation, magnetic hysteresis, pulsed power systems**

I. Introduction

FAST-ramping normal-conducting magnets delivering rise rates of several $\mathrm{kT/s}$ receive increasing attention as they fill various key roles in particle accelerator lattices. A synchrotron-based muon collider will make extensive use of such magnets in the intermediate acceleration stages [1], [2]. The magnets will be excited by periodically pulsed currents with very short duty cycles [3], in order to minimize resistive loss while reliably enforcing the requested ramp-up of the magnetic field.

The ramped excitation and the locally strong saturation of the ferromagnetic yoke prohibit the application of frequency-domain approaches. Moreover, calculating the hysteresis loss by post-processing an anhysteretic solution, e.g. by the Steinmetz-Bertotti formulae [4], yields inaccurate results as overall energy conservation and the time-lag between exciting current and generated magnetic field are neglected. In order to precisely resolve the ferromagnetic behavior of hysteresis and eddy-current phenomena, an adequate dynamic material model as in [5], [6] will be formulated and applied.

In the following sections, the numerical representations of Maxwell's equation and the applied dynamic energy-based hysteresis model are introduced. The proposed method is then successfully applied on one of the current designs of a fast-ramping muon-collider magnet. Lastly, the computational costs are compared and discussed.

II. Formulation and Discretization

The magnetic vector potential approach resolves the magnetic law of Gauss and the law of Faraday-Lenz as

$$\mathbf{B} = \nabla \times \mathbf{A}, \tag{1}$$

$$\mathbf{E} = -\dot{\mathbf{A}} - \nabla\varphi, \tag{2}$$

with magnetic flux density $\mathbf{B}(\mathbf{r},t)$, electric field strength $\mathbf{E}(\mathbf{r},t)$, magnetic vector potential $\mathbf{A}(\mathbf{r},t)$ and electric scalar potential $\varphi(\mathbf{r},t)$. With current density $\mathbf{J} = \sigma\mathbf{E}$ we formulate the law of Ampère as

$$\nabla \times \mathbf{H} + \sigma\dot{\mathbf{A}} = -\sigma\nabla\varphi, \tag{3}$$

with $\mathbf{H}(\mathbf{r},t)$ the magnetic field strength and $\sigma(\mathbf{r})$ the conductivity. A so-called field-circuit coupling is needed to account for the external circuitry creating the pulse. Every conductor is given a distribution function $\mathbf{x}_m(\mathbf{r})$ [7] of dimension m^{-1} such that

$$-\sigma\nabla\varphi = \sum_m u_m \sigma \mathbf{x}_m, \tag{4}$$

where $u_m(t)$ are the voltages along the conductors. The currents through the solid conductors are given by

$$i_m = G_m u_m - (\mathbf{x}_m, \sigma\dot{\mathbf{A}})_\Omega, \tag{5}$$

where $G_m = (\mathbf{x}_m, \sigma\mathbf{x}_m)_\Omega$ is the conductance of conductor m and $(\cdot,\cdot)_\Omega$ denotes the L^2 scalar product over the computational domain Ω. The variational form of (3) is

$$(\mathbf{v},\mathbf{H})_\Omega + \cancelto{0}{(\mathbf{H}\times\mathbf{v},\mathbf{n})_{\partial\Omega}} + (\mathbf{w},\sigma\dot{\mathbf{A}})_\Omega = \sum_m u_m(\mathbf{w},\sigma\mathbf{x}_m)_\Omega, \tag{6}$$

where the test function $\mathbf{w}$ belongs to the space $H(\mathrm{curl},\Omega)$ of tangentially continuous vector fields with vanishing tangential components at the Dirichlet boundaries, and $\mathbf{v} = \nabla\times\mathbf{w}$.

Adopting the Ritz-Galerkin approach, i.e., using the same functions $\mathbf{w}_n$ for discretizing $\mathbf{A} \approx \sum_n a_n(t)\mathbf{w}_n$ and testing one obtains

$$\widehat{\mathbf{h}}(\mathbf{a},\dot{\mathbf{a}}) + \mathbf{M}_\sigma\dot{\mathbf{a}} = \mathbf{X}\mathbf{u}, \tag{7}$$

with $\widehat{h}_j = (\mathbf{v}_j,\mathbf{H})_\Omega$, $\mathbf{M}_\sigma|_{j,k} = (\mathbf{w}_j,\sigma\mathbf{w}_k)_\Omega$, $\mathbf{X}|_{j,m} = (\mathbf{w}_j,\sigma\mathbf{x}_m)_\Omega$. In case of known current excitations the system can be reformulated by incorporating (5)

$$\widehat{\mathbf{h}}(\mathbf{a},\dot{\mathbf{a}}) + (\mathbf{M}_\sigma - \mathbf{X}\mathbf{R}\mathbf{X}^\top)\dot{\mathbf{a}} = \mathbf{X}\mathbf{R}\mathbf{i}, \tag{8}$$

with $\mathbf{R}|_{j,m} = R_m\delta_{jm}$ as diagonal matrix of all resistances.

Manuscript received December 1, 2012; revised August 26, 2015. Corresponding author: D. Moll (email: dominik.moll1@tu-darmstadt.de).

The right hand side of (7) (or selectively (8)) is known for all times. A Newton based solving scheme expands the left hand side locally around a guess $\mathbf{a}'$, $\dot{\mathbf{a}}'$

$$\widehat{\mathbf{h}}(\mathbf{a},\dot{\mathbf{a}}) + \mathbf{M}_\sigma \dot{\mathbf{a}} \approx \widehat{\mathbf{h}}(\mathbf{a}',\dot{\mathbf{a}}') + \mathbf{M}_\sigma \dot{\mathbf{a}}' + \frac{\partial \widehat{\mathbf{h}}'}{\partial \mathbf{a}}\delta\mathbf{a} + \left(\frac{\partial \widehat{\mathbf{h}}'}{\partial \dot{\mathbf{a}}} + \mathbf{M}_\sigma\right)\delta\dot{\mathbf{a}}, \quad (9)$$

with $\delta\dot{\mathbf{a}} = \dot{\mathbf{a}} - \dot{\mathbf{a}}'$, $\delta\mathbf{a} = \mathbf{a} - \mathbf{a}'$ and

$$\frac{\partial \widehat{h}_j}{\partial a_k} = \left(\mathbf{v}_j, \frac{\partial \mathbf{H}}{\partial a_k}\right)_\Omega = \left(\mathbf{v}_j, \frac{\partial \mathbf{H}}{\partial \mathbf{B}}\mathbf{v}_k\right)_\Omega,$$
$$\frac{\partial \widehat{h}_j}{\partial \dot{a}_k} = \left(\mathbf{v}_j, \frac{\partial \mathbf{H}}{\partial \dot{a}_k}\right)_\Omega = \left(\mathbf{v}_j, \frac{\partial \mathbf{H}}{\partial \dot{\mathbf{B}}}\mathbf{v}_k\right)_\Omega.$$

Within the scope of this paper we will expect $\frac{\partial \mathbf{H}}{\partial \dot{\mathbf{B}}}$ to be constant, such that the system of differential equations is given in explicit form $\mathbf{M}\dot{\mathbf{a}} = \mathbf{f}(t,\mathbf{a})$ and standard time-integration routines can be applied. We use the in-house Python package `Pyrit` [8] to assemble all finite element systems.

III. Magnetic Constitutive Laws

On the macroscopic scale the magnetic flux density and the magnetic field strength are related via the magnetization $\mathcal{M} : \mathbf{H} \mapsto \mathbf{M}$

$$\mathbf{B} = \mu_0(\mathbf{H} + \mathbf{M}(\mathbf{H})) = (\mu_0 + \mu_0\mathcal{M})\mathbf{H}. \quad (10)$$

In this section we characterize the ferromagnetic response of the M235-35A soft-magnetic alloy, which will serve as iron yoke material in the accelerator magnet design. Extensive measurement data on this material can be found and was used in the frame of this work [9], [10], [11].

A. Anhysteretic Material Response

The anhysteretic magnetization shall be given by an isotropic relationship as in [9]

$$|\mu_0\mathbf{M}_{\text{an}}| = \mu_0 M_a L(\frac{|\mathbf{H}|}{h_a}) + \mu_0 M_b L(\frac{|\mathbf{H}|}{h_b}), \quad (11)$$

with Langevin function $L(x) = \coth(x) - x^{-1}$, $\mu_0 M_a = 1.39\,\text{T}$, $h_a = 18.18\,\text{A/m}$, $\mu_0 M_b = 0.56\,\text{T}$, $h_b = 3.91\,\text{kA/m}$. The maximum susceptibility of $\chi_{\max} = 20.32\ 10^3$ is found for very small excitations $|\mu_0\mathbf{M}_{\text{an}}| = \mu_0\chi_{\max}|\mathbf{H}| + \mathcal{O}(|\mathbf{H}|^3)$.

Anhysteretic models are commonly applied as they offer a rapid evaluation of $\mathbf{H} \mapsto \mathbf{B}$ and also $\mathbf{B} \mapsto \mathbf{H}$, whereby the latter may require the use of look-up-tables as analytical inverses often can not be provided. Similarly straight forward is the construction of the differential tensors

$$\frac{\partial \mu_0\mathbf{M}_{\text{an}}}{\partial \mathbf{H}} = \frac{|\mu_0\mathbf{M}_{\text{an}}|}{|\mathbf{H}|}[\mathbf{I} - \mathbf{e}_\mathbf{H}\mathbf{e}_\mathbf{H}^\top] + \frac{\partial |\mu_0\mathbf{M}_{\text{an}}|}{\partial |\mathbf{H}|}\mathbf{e}_\mathbf{H}\mathbf{e}_\mathbf{H}^\top. \quad (12)$$

By construction, this type of material model is incapable of reproducing the hysteretic behavior of ferromagnetic alloys. Accordingly, the hysteresis loss can only be approximated using a posteriori formulae for which we here assume the principle of loss separation [4] combined with signal-independent generalized loss expressions [12]. The time-averaged hysteresis and eddy current loss densities are

$$\bar{p}_{\text{hyst}} = \frac{\int_0^T \gamma k_{\text{hyst}} |\dot{\mathbf{B}}| \hat{B} \mathrm{d}t/T}{\int_0^{2\pi} |2\pi\cos(\theta)| \mathrm{d}\theta/2\pi}, \quad (13)$$

$$\bar{p}_{\text{eddy}} = \frac{\int_0^T \gamma k_{\text{eddy}} |\dot{\mathbf{B}}|^2 \mathrm{d}t/T}{\int_0^{2\pi} |2\pi\cos(\theta)|^2 \mathrm{d}\theta/2\pi}, \quad (14)$$

with mass-density γ, empirically obtained parameters k_{hyst}, k_{eddy} and $\hat{B}$ as one half of the peak to peak value of the local magnetic flux density. The values $k_{\text{hyst}} = 13.88\,\text{mW/(kgHzT}^2\text{)}$ and $k_{\text{eddy}} = 44.77\,\mu\text{W/(kgHz}^2\text{T}^2\text{)}$ have been reported in [10] and are used here. The so-called excess loss will not be discussed in this work.

B. Hysteretic Material Response – Forward

The energy-based hysteresis model of Bergqvist [13] and refined by Henrotte [14] expresses the magnetization as

$$\mathbf{M}(\mathbf{H}) = \sum_k \mathbf{M}_k(\mathbf{H}) = \sum_k w_k \mathcal{M}_{\text{an}} \mathcal{H}_{\text{r}}^k \mathbf{H}, \quad (15)$$

for which the weights w_k fulfill $\sum_k w_k = 1$. The operator $\mathcal{M}_{\text{an}}$ realizes the anhysteretic mapping as defined in III-A. A history dependence is included in the operators $\mathcal{H}_{\text{r}}^k$ which can be approximated by a vector-play model with pinning forces $\kappa_k \geq 0$ and Heaviside function Θ [14]

$$\mathbf{H}_r^k = \mathcal{H}_r^k\mathbf{H} = \mathbf{H}_{r,\text{prev}}^k + f(|\delta\mathbf{H}_k|, \kappa_k)\mathbf{e}_{\delta\mathbf{H}_k}, \quad (16)$$
$$f(x,y) = (x-y)\,\Theta(x-y),$$
$$\delta\mathbf{H}_k = \mathbf{H} - \mathbf{H}_{r,\text{prev}}^k.$$

For unidirectional fields this approximation is fully consistent with the energy conserving framework. For arbitrary fields, errors are introduced by this model which can only be diminished by solving a computationally more expensive optimization problem [16].

For both approaches the computation of the differential susceptibility tensor $\frac{\partial \mathbf{M}}{\partial \mathbf{H}}$ and differential permeability tensor $\frac{\partial \mathbf{B}}{\partial \mathbf{H}} = \mu_0 + \mu_0 \frac{\partial \mathbf{M}}{\partial \mathbf{H}}$ becomes a concatenation of analytical expressions [17]

$$\frac{\partial \mathbf{M}}{\partial \mathbf{H}} = \sum_k w_k \frac{\partial \mathbf{M}_{\text{an}}}{\partial \mathbf{H}_{\text{r}}^k} \frac{\partial \mathbf{H}_{\text{r}}^k}{\partial \mathbf{H}}. \quad (17)$$

The local power density $\mathbf{H}\cdot\dot{\mathbf{B}}$ translates into a change in stored magnetic energy w_{mag} and a hysteretic loss p_{hyst}

$$\dot{w}_{\text{mag}} = \mathbf{H}\cdot\mu_0\dot{\mathbf{H}} + \sum_k \mathbf{H}_r^k \cdot \mu_0 \dot{\mathbf{M}}_k, \quad (18)$$

$$p_{\text{hyst}} = \sum_k \left(\mathbf{H} - \mathbf{H}_r^k\right)\cdot\mu_0\dot{\mathbf{M}}_k \geq 0. \quad (19)$$

Within the scope of this work the vector-play model was selected, as the impact of the thereby introduced errors has been observed to be marginal for our intended application of accelerator magnets for which global losses and aperture field are the main quantities of interest.

Figure 1 illustrates the identified model parameters for M235-35A based on the algorithm and data discussed in [15]. A total of eleven summands $\mathbf{M}_k$ was intentionally selected to balance computational complexity and physical fidelity.

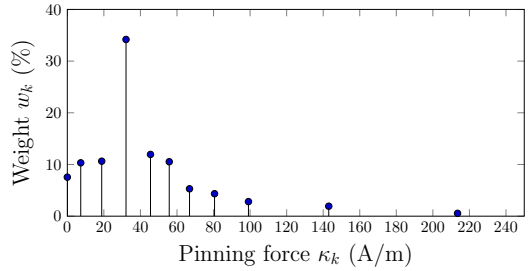

Fig. 1. Weights and pinning forces of M235-35A, based on [15].

C. Hysteretic Material Response – Inverse

The introduced vector-potential based solving algorithm (7) requires the inverse mapping $(\mu_0 + \mu_0\mathcal{M})^{-1} : \mathbf{B} \mapsto \mathbf{H}$. A direct realization of this operation has been recently proposed [18]. State-of-the-art implementations rely on fixed-point iteration schemes based upon the forward model [17].

The fixed-point iteration schemes for a given $\mathbf{B}^*$ are characterized by $\mathcal{Q} : \mathbf{H}, \mathbf{B}^* \mapsto \mathbf{Q}$ such that $\mathbf{H}_{n+1} = \mathbf{Q}(\mathbf{H}_n, \mathbf{B}^*)$ constructs a converging series with $\lim_{n\to\infty} \mathbf{H}_n = \mathbf{H}^*$ and $\mathbf{B}^* = \mathbf{B}(\mathbf{H}^*)$. Root finding algorithms applied on the residual

$$\mathbf{g}(\mathbf{H}^*, \mathbf{B}^*) = \mathbf{B}(\mathbf{H}^*) - \mathbf{B}^* = \mathbf{0} \tag{20}$$

lead to the following iterative schemes

a) Direct Iteration:

$$\mathbf{Q}(\mathbf{H}, \mathbf{B}^*) = \mathbf{H} - (\mu_0\mu_{r,\max})^{-1}\mathbf{g}(\mathbf{H}, \mathbf{B}^*), \tag{21}$$

b) Newton Iteration:

$$\mathbf{Q}(\mathbf{H}, \mathbf{B}^*) = \mathbf{H} - \frac{\partial \mathbf{B}}{\partial \mathbf{H}}^{-1} \mathbf{g}(\mathbf{H}, \mathbf{B}^*). \tag{22}$$

The direct iteration has ensured convergence for all initial guesses $\mathbf{H}_0$ with $\mu_0\mu_{r,\max}$ being the maximum differential permeability but converges slowly. The Newton iteration is able to provide a much faster convergence if the initial guess is well justified for example by using the previous result in combination with a very fine time stepping. As the validity of the initial guess is not a priori known the Newton method generally needs to be stabilized by additional success criteria and relaxation factors. Furthermore, the differential tensors must be constructed for every iteration step.

To overcome the disadvantages of both of these well studied schemes we introduce the preconditioned iteration scheme. The preconditioned residual is defined as

$$\mathbf{g}_p(\mathbf{H}^*, \mathbf{B}^*) = \mathbf{B}_{\text{an}}^{-1}(\mathbf{B}(\mathbf{H}^*)) - \mathbf{B}_{\text{an}}^{-1}(\mathbf{B}^*) = \mathbf{0} \tag{23}$$

yielding the

c) Preconditioned Iteration:

$$\mathbf{Q}(\mathbf{H}, \mathbf{B}^*) = \mathbf{H} - \mathbf{g}_p(\mathbf{H}, \mathbf{B}^*) \tag{24}$$

The preconditioned iteration thus actively exploits information on the anhysteretic magnetization curve $\mathbf{B}_{\text{an}}$ for which the inverse operation can be cheaply performed using look-up-tables. It yields ensured convergence for the ferromagnetic material and drastically reduces the amount of iteration steps as opposed to the direct iteration.

TABLE I
COMPUTATION TIME IN µs PER PROBLEM AND ITERATION COUNT (BOLD)

relative error	$h_0 = 100\,\text{A/m}$ Direct	Newton	Precond.	$h_0 = 1\,\text{kA/m}$ Direct	Precond.
10^{-3}	13.2	10.2	6.3	53.0	7.2
	10	**3**	**4**	**48**	**5**
10^{-6}	25.8	11.8	10.4	64.0	11.3
	22	**4**	**8**	**59**	**9**
10^{-9}	38.0	11.8	15.2	77.1	16.4
	33	**4**	**13**	**70**	**14**

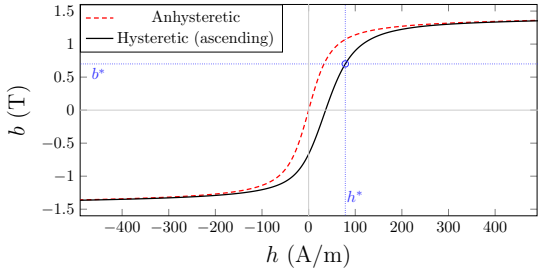

Fig. 2. Anhysteretic and hysteretic material response (ascending branch, major cycle). Input b^* and target h^* of the one-dimensional inverse hysteresis problem.

Identical one-dimensional inverse problems with $\mathbf{B}^* = 0.7\,\text{T}\,\mathbf{e}_\theta$ on the ascending branch of the major hysteresis cycle (Fig. 2) with angular direction $\mathbf{e}_\theta = \cos(\theta)\mathbf{e}_x + \sin(\theta)\mathbf{e}_y$ have been solved for 36000 distinct angles using a serial implementation. Table I displays the averaged runtime per problem and iteration count. The solution is approximately given by $\mathbf{H}^* \approx 78.68\,\text{A/m}\,\mathbf{e}_\theta$. For a comparably good initial guess of $\mathbf{H}_0 = h_0\mathbf{e}_\theta = 100\,\text{A/m}\,\mathbf{e}_\theta$ the Newton iteration performs best in terms of iterations needed and computation time for a strict tolerance of 10^{-9}. For lower tolerances the preconditioned iteration was found to be the fastest scheme. Generally the preconditioned iteration has a time consumption in the same order of magnitude as the Newton scheme. Both methods clearly outperform the direct iteration. For the significantly worse initial guess of $h_0 = 1\,\text{kA/m}$ the iteration count of the preconditioned iteration only rises by one. The Newton method is unable to converge and the time consumption of the direct iteration scheme more than doubles.

The preconditioned iteration scheme describes a computationally inexpensive and stable procedure to realize the inverse hysteretic mapping $\mathbf{B} \mapsto \mathbf{H}$. Unlike the Newton method, it does not necessitate relaxation criteria or sufficiently fine time stepping. Based on these considerations we have concluded to use the preconditioned iteration scheme of up to 20 iteration steps in this work.

D. Dynamic Ferromagnetic Response

The magnetic response of soft-magnetic alloys is further governed by the eddy current problem which in case of purely transversal fields with $\partial_x = \partial_y = 0$ reduces to the so-called one-dimensional lamination problem $-\partial_z^2\mathbf{H} = -\sigma_{\text{Fe}}\dot{\mathbf{B}}$.

It was shown that the dynamic model

$$\mathbf{H}_{\text{surf}} = \mathbf{H}(\mathbf{B}) + \frac{\sigma_{\text{Fe}} d^2}{12}\dot{\mathbf{B}} \tag{25}$$

is able to approximate the magnetic field strength $\mathbf{H}_{\text{surf}}$ at the iron-insulation-interface very well for low frequent periodic excitations [5], [19]. The assumption of $\frac{\partial \mathbf{H}_{\text{surf}}}{\partial \dot{\mathbf{B}}}$ being constant (II) is fulfilled. The eddy current loss is given by

$$p_{\text{eddy}} = \frac{\sigma_{\text{Fe}} d^2}{12}|\dot{\mathbf{B}}|^2 \geq 0. \tag{26}$$

Further refinements of this dynamic model including excess terms have been suggested but are not considered in this scope [6]. In the following section we will apply the anhysteretic and hysteretic material responses with and without the eddy-current contribution of (25).

IV. Application

A. Magnet Layout

A dipole magnet consisting of an angled H-type ferromagnetic yoke and eight solid conductors (Fig. 3) will be analyzed. This particular design is the result of a cost minimizer for the second rapid cycling synchrotron (RCS2) of a potential muon collider [20]. The provided dipole field must be ramped from negative ($-1.8\,\text{T}$) to positive peak ($1.8\,\text{T}$) within $1\,\text{ms}$ [20], [21]. The length measures several meters, such that end effects are of no interest in this initial study and the assumption of purely transversal fields holds (III-D).

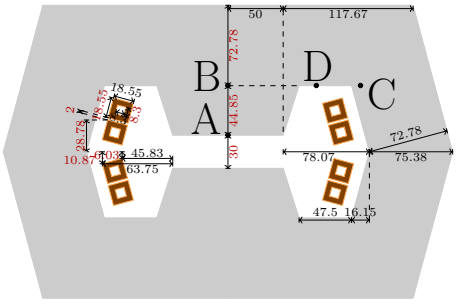

Fig. 3. Analyzed H-type dipole magnet. All lengths in millimeters.

B. Sinusoidal Excitation

We firstly select a sinusoidal current excitation of $I = 12.5\,\text{kA}\sin(2\pi \cdot 500\,\text{Hz} \cdot t + \phi_0)$ per conductor and compare the results of the discussed material models. To accommodate an initial system state without current and without electromagnetic field the initial phase ϕ_0 is considered to be zero. We simulate three periods with 100 equidistant implicit Euler steps per $1\,\text{ms}$ time intervall.

The loss of the third cycle is given by $336.08\,\text{J/m}$ and is heavily dominated by the resistive loss occurring in the copper conductors (Tab. II and Fig. 4). The iron yoke loss contributes less than 20% of the total loss whereby the eddy current loss is more than twice as large as the hysteresis loss.

All used ferromagnetic models agree in terms of resistive loss. The eddy current and hysteresis loss obtained via the

TABLE II
Loss per cycle in J/m for a sinusoidal excitation

Material model	Eddy current	Hysteresis	Resistive
Anhysteretic (static)	47.15 (a post.)	23.54 (a post.)	272.90
Anhysteretic (dynamic)	41.22	0	272.88
Hysteretic (static)	0	20.12	273.41
Hysteretic (dynamic)	42.61	20.09	273.38

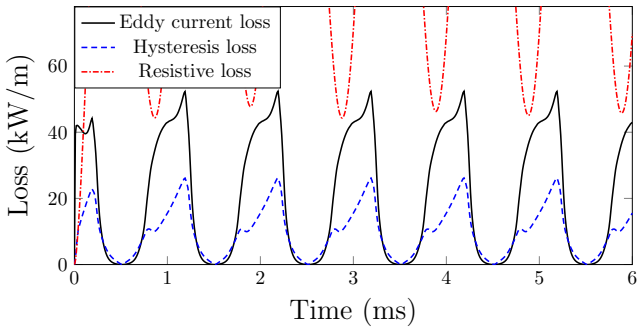

Fig. 4. Loss as obtained by using the dynamic hysteresis model for a sinusoidal excitation.

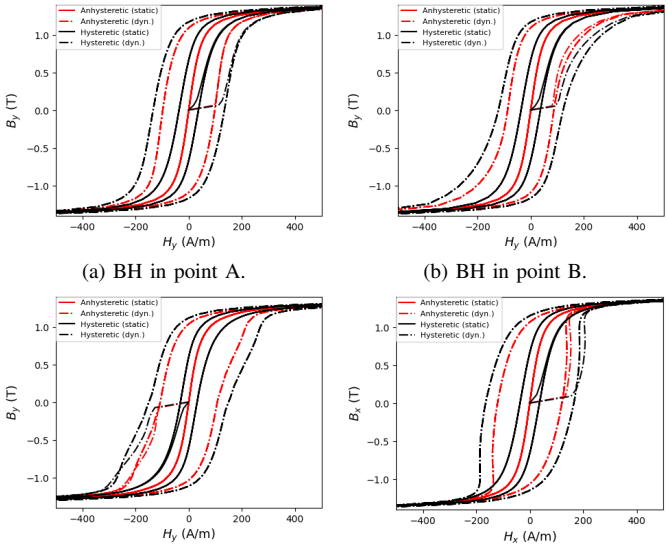

(a) BH in point A. (b) BH in point B.

(c) BH in point C. (d) BH in point D.

Fig. 5. BH loci in the ferromagnetic yoke. Static model: solid lines. Dynamic model: dashed lines.

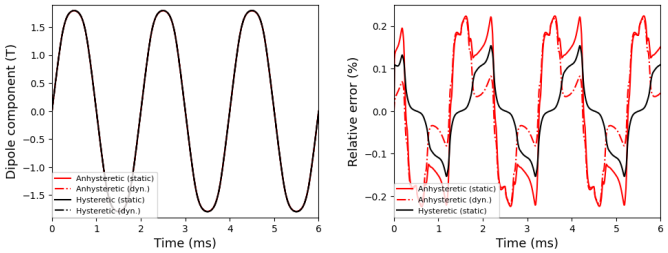

(a) Dipole component. (b) Relative differences of dipole component compared to the dynamic hysteresis model.

Fig. 6. Dipole component in the air gap center.

a posteriori formulae is 11% and 17% larger than with the dynamic hysteresis model. The discrepancy is caused by the a posteriori loss factors k_{eddy} and k_{hyst} which are not tuned for the comparably high frequency of 500 Hz [10]. Our results underline the weaknesses of a posteriori loss estimates and would allow to readjust k_{eddy} and k_{hyst} for this particular frequency.

The BH loci in four yoke points are shown in Fig. 5. The initial state is given by zero. The static loci in all points are almost identical, whereas the dynamic model causes a notably different broadening of the BH loop of each point.

The dipole component in the air gap center (Fig. 6a) is not significantly influenced by the ferromagnetic model. Relative differences in the order of 10^{-3} are observed (Fig. 6b).

C. Triangular Pulsed Excitation

We will now assume an excitation of repeating triangular pulses (Fig. 7) as idealized current supply of the magnet obtained from a switched resonance circuit [3]. In the simulations the intended repetition rate of 5 Hz was increased to 100 Hz in order to shorten the constant zero-phases and thus reduce computational efforts. Again 100 equidistant time steps per 1 ms are applied.

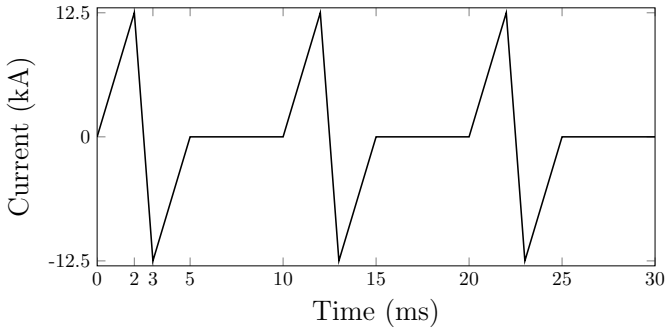

Fig. 7. Triangular pulsed current. The fall rates are four times larger than the rise rates.

The hysteresis loss of the pulsed excitation is identical to the result obtained for the sinusoidal excitation (Tab. III). The eddy current loss is more than halved due to the lower rise and fall rates. The overall loss of one pulse with 358.70 J/m is however higher than for a single sinusoidal period due to an increase of almost 46 J/m in resistive loss. Due to skin- and proximity effects the resistive loss does not instantaneously drop to zero once a pulse terminates. Instead, the resistive loss decays exponentially (Fig. 8).

The BH loci of the dynamic models (Fig. 9) are narrower than for the sinusoidal excitation. The ascending branch encloses a much smaller area than the descending branch, due to significantly different rise and fall rates of the current excitation. We can furthermore identify plateaus at which $\mathbf{B}$ and $\mathbf{H}$ transfer from dynamic to static behavior once a pulse terminates, such as $B_x = 0.4\,\text{T}$ in point D (Fig. 9d).

The resulting aperture field (Fig. 10) again differs by only 0.2%. The most noteworthy difference is the constant remanence field of $-0.75\,\text{mT}$ after each pulse which can only be resolved by the hysteretic models.

TABLE III
LOSS PER CYCLE IN J/m FOR A PULSED EXCITATION

Material model	Eddy current	Hysteresis	Resistive
Anhysteretic (static)	21.63 (a post.)	23.60 (a post.)	318.79
Anhysteretic (dynamic)	18.62	0	318.78
Hysteretic (static)	0	20.14	319.23
Hysteretic (dynamic)	19.38	20.10	319.22

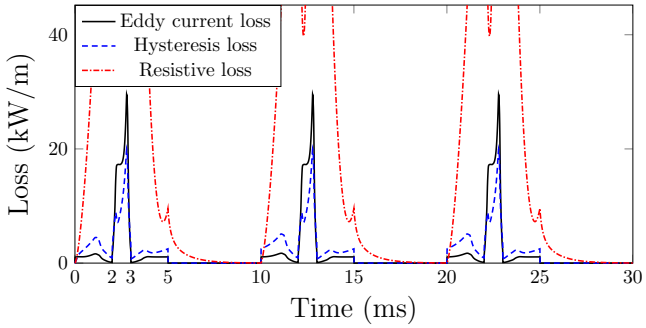

Fig. 8. Loss as obtained by using the dynamic hysteresis model for a pulsed excitation.

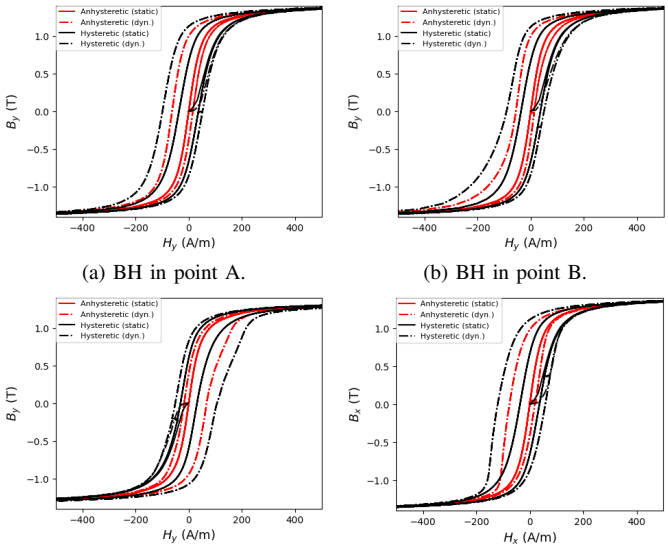

(a) BH in point A. (b) BH in point B.

(c) BH in point C. (d) BH in point D.

Fig. 9. BH loci in the ferromagnetic yoke. Static model: solid lines. Dynamic model: dashed lines.

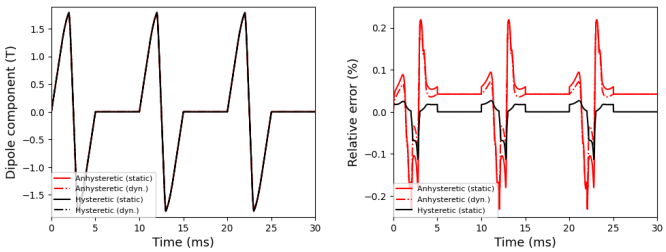

(a) Dipole component. (b) Relative differences of dipole component compared to the dynamic hysteresis model.

Fig. 10. Dipole component in the air gap center.

V. Runtime Comparison

The simulation runtime increases linearly with the timesteps N_t, nonlinear iteration steps N_{Newton} and degrees of freedom N_{Nodes}, i.e., $\mathcal{O}(N_t N_{\text{Newton}} N_{\text{Nodes}})$. The calculations with anhysteretic and hysteretic model only differ in the ferromagnetic material evaluation, which is required in all $N_{\text{int}}^{\text{Fe}}$ integration points of the iron yoke. The additional time consumption related to the serialized material evaluation scales as $\mathcal{O}(N_t N_{\text{Newton}} N_{\text{int}}^{\text{Fe}})$.

The calculation with sinusoidal excitation was repeated for various uniformly resolved meshes using a standard desktop computer with 10 cores and 32 GB of RAM. The amount of time steps and Newton iterations was fixed as $N_t = 600$ and $N_{\text{Newton}} = 5$. The simulation with a mesh of $N_{\text{int}}^{\text{Fe}} = 11898$ integration points required $32.7\,\text{min}$ with anhysteretic materials and $43.5\,\text{min}$ with hysteretic materials (Fig. 11). The difference of $10.8\,\text{min}$ translates into an additional individual evaluation time of $18.2\,\mu\text{s}$ per integration point which is in a good agreement with the results reported in Tab. I.

Since the material evaluations for each integration point are fully independent of another, a parallelization is easily implementable. A dual thread material evaluation reduced the simulation time to $38.3\,\text{min}$ and thus almost halved the time difference. For coarser meshes the speed-up was lower due to the necessarily introduced overhead of the parallelized implementation.

Under idealized circumstances the runtime can be reduced to $\mathcal{O}(N_t N_{\text{Newton}})$ and thus a constant in $N_{\text{int}}^{\text{Fe}}$ by performing all $N_{\text{int}}^{\text{Fe}}$ material evaluations on distinct threads. In this example the additional simulation time would be only $55\,\text{ms}$.

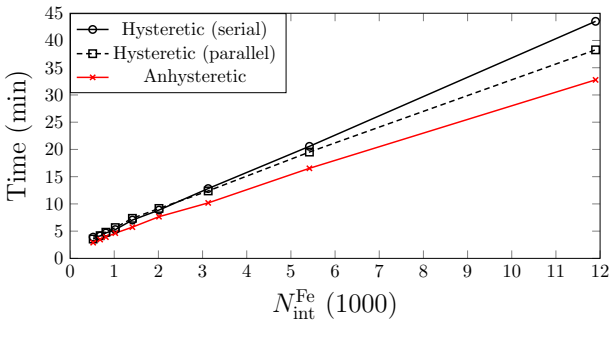

Fig. 11. Runtime for solving the transient FE problem with sinusoidal excitation on uniformly resolved meshes. The parallel material evaluation used two threads.

VI. Conclusion

In this paper, we have presented a new stable and quickly evaluable inversion scheme of the energy-based hysteresis model. The static ferromagnetic model has been extended by the thin sheet eddy-current description to obtain a dynamic hysteresis model. It enabled an accurate simulation of a fast-ramping accelerator magnet for sinusoidal and triangular pulsed current excitations. The resulting differences in fields and loss as compared to a static anhysteretic model were comparably small, granted correctly adjusted loss parameters of the a posteriori formulae. However, the dynamic hysteresis model is the only analyzed option actively incorporating eddy current and hysteresis loss in the time domain simulation. This property is crucial when analyzing the behavior of switched resonance circuits consisting of capacitor banks and magnets. We have shown that the added computational complexity in terms of material evaluation time is manageable and can even on standard machines be reduced by exhausting parallelization.

Acknowledgment

This work is funded by the European Union (EU) within the Horizon Europe Framework Programme (Project MuCol, grant agreement 101094300). Views and opinions expressed are however those of the author(s) only and do not necessarily reflect those of the EU or European Research Executive Agency (REA). Neither the EU nor the REA can be held responsible for them. Endorsed by the IMCC.

References

[1] L. Bottura et al., "Magnets for a Muon Collider—Needs and Plans", *IEEE Trans. Appl. Supercond.*, vol. 34, no. 5, pp. 1-8, 2024.
[2] J. S. Berg et al., "Pulsed synchrotrons for very rapid acceleration", *AIP Conf. Proc.*, 2016.
[3] D. Aguglia et al., "A two harmonics circuit for the powering of the very fast RCS (Rapid Cycling Synchrotron) of the muon collider accelerator", *Proc. IPAC'23*, Venice, Italy, May 2023, pp. 3746-3749.
[4] G. Bertotti, "General properties of power losses in soft ferromagnetic materials", *IEEE Trans. Magn.*, vol. 24, no. 1, pp. 621-630, 1988.
[5] J. Gyselinck et al.,"Calculation of eddy currents and associated losses in electrical steel laminations", *IEEE Trans. Magn.*, vol. 35, no. 3, pp. 1191-1194, 1999.
[6] S.E. Zirka et al., "Dynamic Hysteresis Modeling", *Physica B: Condensed Matter*, vol. 343, pp. 90-95, 2004.
[7] S. Schöps et al., "Winding functions in transient magnetoquasistatic field-circuit coupled simulations", *COMPEL*, vol. 32, no. 6, pp. 2063–2083, Nov. 2013.
[8] J. Bundschuh et al.,"Pyrit: A finite element based field simulation software written in Python", *COMPEL*, vol. 42, no. 5, pp. 1007-1020, 2023.
[9] S. Steentjes et al., "A dynamical energy-based hysteresis model for iron loss calculation in laminated cores" *Int. J. Numer. Model.*, vol 27, pp. 433-443, 2014.
[10] D. Eggers et al., "Advanced Iron-Loss Estimation for Nonlinear Material Behavior", *IEEE Trans. Magn.*, vol. 48, no. 11, pp. 3021-3024, 2012.
[11] F. Henrotte et al.,"Iron Loss Calculation in Steel Laminations at High Frequencies", *IEEE Trans. Magn.*, vol. 50, no. 2, pp. 333-336, 2014.
[12] K. Venkatachalam et al., "Accurate prediction of ferrite core loss with nonsinusoidal waveforms using only Steinmetz parameters", 2002 IEEE Workshop on Computers in Power Electronics, 2002. Proceedings., Mayaguez, PR, USA, 2002, pp. 36-41.
[13] A. Bergqvist, "Magnetic vector hysteresis model with dry friction-like pinning", *Physica B*, 233:342–347, 1997.
[14] F. Henrotte et al., "An energy-based vector hysteresis model for ferromagnetic materials", *COMPEL*, 25:71–80, 2006.
[15] K. Jacques, "Energy-Based Magnetic Hysteresis Models", Ph.D. dissertation, Université de Liège, 2018.
[16] L. Prigozhin et al., "On the Energy-Based Variational Model for Vector Magnetic Hysteresis", *IEEE Trans. Magn.*, vol. 52, no. 12, pp. 1-11, 2016.
[17] K. Jacques et al., "Inclusion of a Direct and Inverse Energy-Consistent Hysteresis Model in Dual Magnetostatic Finite-Element Formulations", *IEEE Trans. Magn.*, vol. 52, no. 3, pp. 1-4, 2016.
[18] H. Egger et al.,"On Forward and Inverse Energy-Based Magnetic Vector Hysteresis Operators", *IEEE Trans. Magn.*, vol. 61, no. 4, pp. 1-7, 2025.
[19] P. Dular et al., "A 3-D magnetic vector potential formulation taking eddy-currents in lamination stacks into account", *IEEE Trans. Magn.*, vol. 39, no. 3, pp. 1424–1427, 2003.
[20] C. Accettura et al., "Interim report for the International Muon Collider Collaboration", arxiv:2407.12450, 2024.
[21] M. Breschi et al., "Comparative Analysis of Resistive Dipole Accelerator Magnets for a Muon Collider", *IEEE Transactions on Applied Superconductivity*, vol. 34, no. 5, pp. 1-5, 2024.